

## Magneto spectroscopy of two-dimensional HgTe-based topological insulators around the critical thickness

M. Zholudev,<sup>1,2</sup> F. Teppe,<sup>1,\*</sup> M. Orlita,<sup>3</sup> C. Consejo,<sup>1</sup> J. Torres,<sup>4</sup> N. Dyakonova,<sup>1</sup> M. Czapkiewicz,<sup>5</sup> J. Wróbel,<sup>5</sup> G. Grabecki,<sup>5</sup> N. Mikhailov,<sup>6</sup> S. Dvoretzkii,<sup>6</sup> A. Ikonnikov,<sup>2</sup> K. Spirin,<sup>2</sup> V. Aleshkin,<sup>2</sup> V. Gavrilenko,<sup>2</sup> and W. Knap<sup>1</sup>

<sup>1</sup>Laboratoire Charles Coulomb (L2C), UMR CNRS 5221, GIS-TERALAB, Université Montpellier II, 34095 Montpellier, France

<sup>2</sup>Institute for Physics of Microstructures, Russian Academy of Sciences, Nizhny Novgorod, Russia

<sup>3</sup>Laboratoire National des Champs Magnétiques Intenses, CNRS-UJF-UPS-INSA, 25, avenue des Martyrs, FR-38042 Grenoble, France

<sup>4</sup>Institut d'Électronique du Sud, UMR 5214 CNRS, Université Montpellier 2, 34095 Montpellier, France

<sup>5</sup>Polish Academy of Sciences, Institute of Physics, aleja Lotników 32/46, Warszawa 02-668, Poland

<sup>6</sup>A.V. Rzhanov Institute of Semiconductor Physics, Siberian Branch, Russian Academy of Sciences, Novosibirsk 630090, Russia

(Received 20 June 2012; revised manuscript received 8 September 2012; published 16 November 2012)

Recently, a new class of materials, so-called topological insulators, has emerged. These are systems characterized by the inversion of the electronic band structure and also by a certain strength of the spin-orbit interaction. HgTe/Cd<sub>x</sub>Hg<sub>1-x</sub>Te quantum wells represent a prominent example. They can change to the topological insulator phase from the conventional insulator phase when the thickness of the quantum well is increased over the critical thickness  $d_c = 6.3$  nm. Here, we report on a far-infrared magneto spectroscopy study of a set of HgTe/Cd<sub>x</sub>Hg<sub>1-x</sub>Te quantum wells with different thicknesses from below to above the critical value  $d_c$ . In quantizing magnetic fields up to 16 T, both intraband and interband transitions have been clearly observed. In the widest quantum well with inverted band structure, we confirm the avoided crossing of the zero-mode Landau levels observed earlier in similar structures. In both noninverted quantum wells close to the critical thickness, we report unambiguously on the square root dependence of the transition energy on the magnetic field, as expected in the single-particle model of massless Dirac fermions. The obtained results are compared with the allowed transition energies between Landau levels in the valence and conduction bands calculated using the  $8 \times 8$  Kane model.

DOI: [10.1103/PhysRevB.86.205420](https://doi.org/10.1103/PhysRevB.86.205420)

PACS number(s): 78.66.Hf, 73.61.Ga

### I. INTRODUCTION

Surface states in semiconducting and insulating materials are usually fragile with respect to disorder and perturbations such as impurity scattering, many-body interactions, and geometrical effects. However, there are systems in which surface states are robust due to the topology of the band structure in the material volume. A well-known example is the integer quantum Hall effect in two-dimensional systems. More recently, another type of topological invariance was predicted in materials with band inversion (semiconductor with a gap between the upper  $p$ -type and lower  $s$ -type energy bands) due to strong spin-orbit coupling.<sup>1</sup> In this case, one speaks of topological insulators.<sup>2</sup>

This kind of topologically protected surface state was first demonstrated to exist in two-dimensional HgTe/CdTe quantum wells (QWs).<sup>3,4</sup> In QWs wider than a critical thickness  $d_c = 6.3$  nm ( $d > d_c$ ), the electronic structure in the well remains inverted. However, for narrow wells ( $d < d_c$ ), it is possible to obtain a conventional alignment of the quantum well states. So, a topological quantum phase transition occurs at the critical thickness  $d_c$ , where the system is described by a massless Dirac theory. In contrast to graphene,<sup>5</sup> where two valleys of Dirac fermions exist, in this new material Dirac fermions appear only at a single point in the Brillouin zone. In QWs of critical thickness, the electron energy depends linearly on its momentum and under applied magnetic field the Dirac energy spectrum evolves into Landau levels with energies having a square root dependence on the magnetic field ( $B$ ). The presence of a band inversion in the HgTe quantum well leads to the existence of topologically protected edge states in which propagation with given  $k$  is linked to the spin

orientation.<sup>1</sup> As a result, these states are robust with respect to time-reversal symmetry invariant scattering processes. Under applied magnetic field, a particular pair (zero-mode) of Landau levels (LLs) splits from the upper and lower energy bands. In the case of inverted band structure these LLs cross at a certain field  $B_c$ , above which the topologically insulating phase is transformed into the conventional quantum Hall insulator phase.<sup>4</sup> So far, there have been no systematic magneto spectroscopy studies of HgTe/CdTe QW heterostructures versus QW width. In Ref. 6, the spectra in two [013]-oriented HgTe samples with a QW width of 7 and 8 nm for different levels of electron concentration were investigated. In Ref. 7, two different samples, each containing a 8-nm-wide [001]-oriented HgTe quantum well, were studied. The field evolution of the particular pair of Landau levels was studied by far-infrared magneto spectroscopy. It was shown that these zero-mode Landau levels in HgTe quantum wells with the inverted band structure do not cross, but instead display the effect of the avoided crossing.

In this paper, we study a set of four samples of different quantum well width by far-infrared magneto spectroscopy from below to above the critical thickness  $d_c$ . Two studied specimens (with wider QWs) have inverted electronic band structures, the other two remain in the noninverted regime. In quantizing magnetic fields up to 16 T, both intraband and interband transitions have been observed. In the group of samples with inverted band structures, we confirm the observation of the avoided crossing of the zero-mode Landau levels at a critical value of the magnetic field. In the group with noninverted band structures, close to the critical thickness, we report on the square root dependence of the intraband transition energy on the magnetic field, as expected in the single-particle model

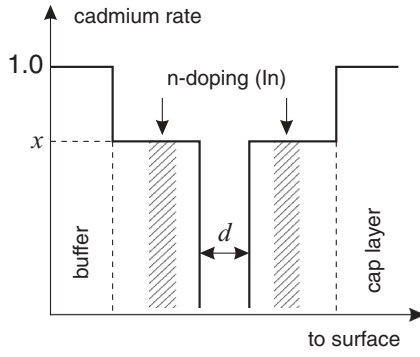


FIG. 1. Schematic drawing of the quantum wells showing the cadmium rate ( $x$ ) in the samples from the buffer to the surface.  $d$  is the QW thickness.

of massless Dirac fermions. Therefore, the results summarized in this paper are divided into two parts related to the physical phenomena mentioned above.

## II. MATERIALS AND METHODS

We have studied four different samples, containing [013]-oriented HgTe QWs from 5.6 up to 8 nm wide embedded in between  $\text{Cd}_x\text{Hg}_{1-x}\text{Te}$  barriers. The samples were grown by molecular beam epitaxy (MBE) on semi-insulating GaAs [013] substrates with relaxed CdTe buffers.<sup>8</sup> A schematic drawing of the structures, showing the cadmium concentration in the layers, is given in Fig. 1.

The band structure of QWs in two samples was inverted. The 8- and 7-nm-wide QWs denoted here as A ( $x = 0.7$ ) and B ( $x = 0.72$ ) were  $n$ -type doped and their dark two-dimensional (2D) electron concentrations were  $2.5 \times 10^{11}$  and  $1.9 \times 10^{11} \text{ cm}^{-2}$ , respectively (cf. Ref. 6). The two other, 5.6- and 5.9-nm-wide quantum wells, denoted, respectively, C ( $x = 0.62$ ) and D ( $x = 0.62$ ) were not intentionally doped and their dark 2D electron concentrations were, however,  $7.8 \times 10^{10}$  and  $2.8 \times 10^{10} \text{ cm}^{-2}$ , respectively. The quantum well widths for the samples C and D indicated during growth were 6 and 7.1 nm, respectively. However, these values do not correspond to the collected experimental data. In particular, the interband transitions are extremely sensitive to the energy band gap and to the QW thickness. The C and D samples have mutually comparable growth parameters; nevertheless, they were grown 18 months after the A and B samples. The calibration of the thickness might change during this period. Indeed, the C and D samples appear to be narrower as compared to the growth indicated values. Instead, the values  $d = 5.6 \text{ nm}$  and  $d = 5.9 \text{ nm}$ , respectively, are the best to fit the experimental data with our calculations. Table I shows an overview of the different samples including QW width and cadmium concentration in the barriers.

In sample A, the longitudinal and Hall resistances have been measured at pumping helium temperatures as a function of the magnetic field and without light exposition. The Hall concentration and mobility were measured at  $2.5 \pm 0.1 \times 10^{11} \text{ cm}^{-2}$  and  $9.9 \pm 0.2 \text{ m}^2/\text{V s}$ , respectively, at  $T = 4.2 \text{ K}$ .

As seen in Fig. 2(a), the Hall resistance shows pronounced plateaus, which correspond well to the values  $R_{xy} = h/ie^2$ , where  $i = 1, 2, 3, 4, \dots$ . In contrast to the wide-gap

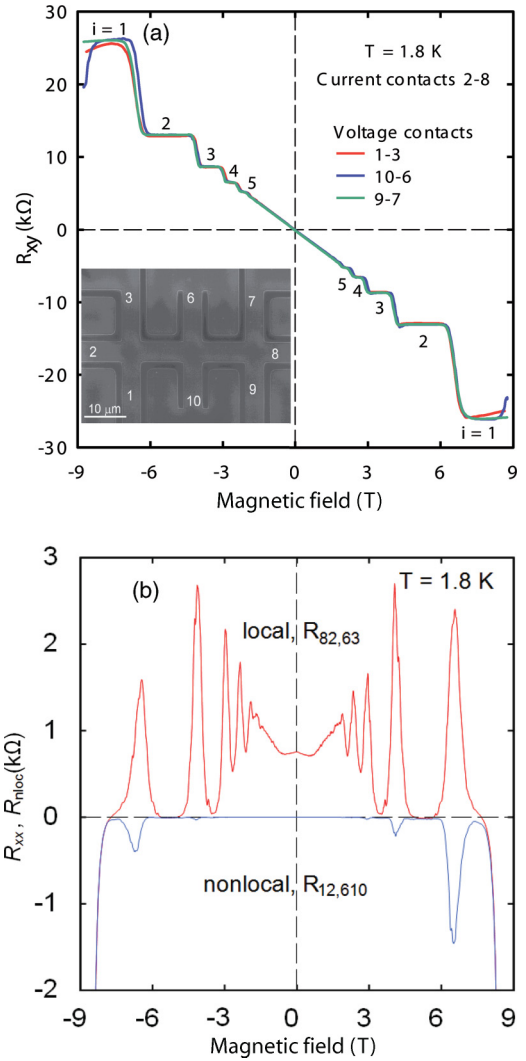


FIG. 2. (Color online) (a) Hall resistance measured for three different pairs of Hall contacts. Consecutive numbers denote plateau indices. Insert shows the geometry of the microstructure patterned on A for transport measurements. The wire ends are connected to large contact pads (not shown here). Indium contacts are soldered to the pads. (b) Longitudinal resistance  $R_{xx} \equiv R_{82,63}$ , as compared with the nonlocal resistance  $R_{nloc} \equiv R_{12,610}$  ( $R_{12,610}$  denotes that the current is passed between probes 1 and 2, and the voltage is measured between 6 and 10).

two-dimensional systems, we observe the plateaus for both even and odd indices  $i$ . They are of similar widths because in our narrow-gap system the spin splitting is comparable to the Landau splitting [see Fig. 2(a)]. Visible slope of the plateau  $i = 1$  (between 6 and 9 T), is probably related to finite resistance of the barrier and/or the substrate materials, leading to some parasite current, parallel to the HgTe quantum well.<sup>9</sup> We estimate this parallel resistance to be in the megohm range. However, the  $R_{xy}$  data show that the quantum well is of high quality and very homogeneous. The oscillations of the longitudinal resistance,  $R_{xx}$  seen in Fig. 2(b), are symmetric with respect to positive and negative values of the applied magnetic field. This also indicates the high material homogeneity. Negative values of  $R_{xx}$  are nevertheless observed at high fields (above  $\pm 8 \text{ T}$ ). This effect can again

TABLE I. Overview of the four samples showing QW thickness, cadmium concentration in the barriers, doping, and dark concentration of 2D electrons.

Sample name	QW thickness, $d$ (nm)	Barrier cadmium rate, $x$	Doping	Dark concentration (cm <sup>-2</sup> )
A	8	0.7	Yes	$2.5 \times 10^{11}$
B	7	0.72	Yes	$1.9 \times 10^{11}$
C	5.6	0.62	No	$7.8 \times 10^{10}$
D	5.9	0.62	No	$2.8 \times 10^{10}$

be attributed to some parallel resistance in the sample. The nonlocal resistance also shown in Fig. 2(b) exhibits maxima as expected for the quantum Hall regime (excluding the negative values above  $\pm 8$  T). Using other combinations of the measuring probes shows very similar results.

In order to measure the infrared transmittance, the sample was exposed to the radiation of a Globar lamp, which was analyzed by a Fourier transform spectrometer and delivered to the sample via light-pipe optics. The transmitted light was detected by a composite bolometer, which operated at  $T = 4.2$  K and was placed directly below the sample. The magneto-optical spectra were measured in Faraday configuration using a superconducting coil ( $B$  up to 11 T in Grenoble and up to 16 T in Montpellier, spectral resolution of 0.5 meV). All the spectra presented here were normalized by the sample transmission at  $B = 0$  and then divided by the rate of reference signals (signal without sample) at nonzero and zero magnetic field. The latter have been done to eliminate slope caused by the influence of the field on the bolometer.

### III. THEORETICAL BASIS

The dispersion of Landau levels was calculated within axial approximation in the manner described in Ref. 10. We use envelope-function approximation and expand the wave function over the same eight basis functions as in Ref. 10. Thus wave function is described by a vector of eight envelope functions. Each of them is a product of some function  $f(z)$  and a lateral function  $\varphi(x,y)$ . In axial approximation lateral functions are equal to those for free electrons in the magnetic field:

$$\varphi(x,y) = \varphi_{n,m}(x,y),$$

where  $n$  is the number of the Landau level and  $m$  is some number responsible for level degeneracy. The explicit form of  $\varphi_{n,m}(x,y)$  depends on the calibration used. These functions are assumed to be zero for  $n < 0$ .

Since total wave function must represent an eigenstate of an axially symmetric Hamiltonian, the number of Landau level for each of the eight components depends on the corresponding Bloch function as follows:<sup>10</sup>

$$\Psi_{n,m,i}(x,y,z) = \begin{pmatrix} \varphi_{n,m}(x,y) \cdot f_{i,1}(z) \\ \varphi_{n+1,m}(x,y) \cdot f_{i,2}(z) \\ \varphi_{n-1,m}(x,y) \cdot f_{i,3}(z) \\ \varphi_{n,m}(x,y) \cdot f_{i,4}(z) \\ \varphi_{n+1,m}(x,y) \cdot f_{i,5}(z) \\ \varphi_{n+2,m}(x,y) \cdot f_{i,6}(z) \\ \varphi_{n,m}(x,y) \cdot f_{i,7}(z) \\ \varphi_{n+1,m}(x,y) \cdot f_{i,8}(z) \end{pmatrix}, \quad (1)$$

where  $i$  is the number used to distinguish levels with the same  $n$  but different energy (e.g., levels from different size quantization subbands).

One can use any values of  $n$  for which at least one component of vector (1) is nonzero (i.e., the first index of function  $\varphi$  is non-negative). The possible values are  $n = -2, -1, 0, 1$ , etc.

The Hamiltonian has been changed according to Ref. 11 in order to describe [013]-oriented heterostructures. The Zeeman term was found to be negligible for our structures and dropped. Taking into account the strain energy, in terms of Ref. 10 the Hamiltonian is

$$\mathbf{H} = \begin{pmatrix} T & 0 & -\frac{1}{\sqrt{2}}Pk_+ & \sqrt{\frac{2}{3}}Pk_z & \frac{1}{\sqrt{6}}Pk_- & 0 & -\frac{1}{\sqrt{3}}Pk_z & -\frac{1}{\sqrt{3}}Pk_- \\ 0 & T & 0 & -\frac{1}{\sqrt{6}}Pk_+ & \sqrt{\frac{2}{3}}Pk_z & \frac{1}{\sqrt{2}}Pk_- & -\frac{1}{\sqrt{3}}Pk_+ & \frac{1}{\sqrt{3}}Pk_z \\ -\frac{1}{\sqrt{2}}k_-P & 0 & U+V & -\bar{S}_- & R & 0 & \frac{1}{\sqrt{2}}\bar{S}_- & -\sqrt{2}R \\ \sqrt{\frac{2}{3}}k_zP & -\frac{1}{\sqrt{6}}k_-P & -\bar{S}_-^+ & U-V & C & R & \sqrt{2}V & -\sqrt{\frac{3}{2}}\bar{S}_- \\ \frac{1}{\sqrt{6}}k_+P & \sqrt{\frac{2}{3}}k_zP & R^+ & C^+ & U-V & \bar{S}_-^+ & -\sqrt{\frac{3}{2}}\bar{S}_+ & -\sqrt{2}V \\ 0 & \frac{1}{\sqrt{2}}k_+P & 0 & R^+ & \bar{S}_+ & U+V & \sqrt{2}R^+ & \frac{1}{\sqrt{2}}\bar{S}_+ \\ -\frac{1}{\sqrt{3}}k_zP & -\frac{1}{\sqrt{3}}k_-P & \frac{1}{\sqrt{2}}\bar{S}_-^+ & \sqrt{2}V & -\sqrt{\frac{3}{2}}\bar{S}_+^+ & \sqrt{2}R & U-\Delta & C \\ -\frac{1}{\sqrt{3}}k_+P & \frac{1}{\sqrt{3}}k_zP & -\sqrt{2}R^+ & -\sqrt{\frac{3}{2}}\bar{S}_-^+ & -\sqrt{2}V & \frac{1}{\sqrt{2}}\bar{S}_+^+ & C^+ & U-\Delta \end{pmatrix},$$

where

$$T = E_c + \frac{\hbar^2}{2m_0} [(2F + 1)(k_x^2 + k_y^2) + k_z(2F + 1)k_z] + a_c(2\varepsilon_{xx} + \varepsilon_{zz}),$$

$$U = E_v - \frac{\hbar^2}{2m_0} [\gamma_1(k_x^2 + k_y^2) + k_z\gamma_1k_z] + a_v(2\varepsilon_{xx} + \varepsilon_{zz}),$$

$$V = -\frac{\hbar^2}{2m_0} \left[ \gamma_2k_x^2 + \left( \frac{23}{50}\gamma_2 + \frac{27}{50}\gamma_3 \right) k_y^2 - \frac{18}{25}k_y\{\gamma_2 - \gamma_3, k_z\} - k_z \left( \frac{73}{50}\gamma_2 + \frac{27}{50}\gamma_3 \right) k_z \right] \\ + \left( \frac{73}{100}b + \frac{9\sqrt{3}}{100}d \right) (\varepsilon_{xx} - \varepsilon_{zz}) + \left( \frac{18}{25}b - \frac{6\sqrt{3}}{25}d \right) \varepsilon_{yz},$$

$$R = -\frac{\hbar^2}{2m_0} \sqrt{3} \left[ -\gamma_2k_x^2 + 2i\gamma_3k_xk_y + \gamma_2k_y^2 + \left( \frac{41}{50}\gamma_2 + \frac{9}{50}\gamma_3 \right) k_y^2 + \frac{6}{25}k_y\{(\gamma_2 - \gamma_3), k_z\} + \frac{9}{50}k_z(\gamma_2 - \gamma_3)k_z \right] \\ + \left( \frac{9}{100}d - \frac{9\sqrt{3}}{100}b \right) (\varepsilon_{xx} - \varepsilon_{zz}) + \left( \frac{6\sqrt{3}}{25}b - \frac{6}{25}d \right) \varepsilon_{yz},$$

$$\bar{S}_{\pm} = -\frac{\hbar^2}{2m_0} \sqrt{3} \left[ k_x\{\gamma_3, k_z\} + k_x\{\kappa, k_z\} \pm \frac{12i}{25}(\gamma_2 - \gamma_3)k_y^2 \pm \frac{i}{25}k_y\{(16\gamma_3 + 9\gamma_2), k_z\} \pm ik_y\{\kappa, k_z\} \mp \frac{12i}{25}k_z(\gamma_2 - \gamma_3)k_z \right] \\ \pm \frac{6i}{25}(\sqrt{3}b - d)(\varepsilon_{xx} - \varepsilon_{zz}) \pm \frac{i}{25}(9\sqrt{3}b + 16d)\varepsilon_{yz},$$

$$\tilde{S}_{\pm} = -\frac{\hbar^2}{2m_0} \sqrt{3} \left[ k_x\{\gamma_3, k_z\} - \frac{1}{3}k_x\{\kappa, k_z\} \pm \frac{12i}{25}(\gamma_2 - \gamma_3)k_y^2 \pm \frac{i}{25}k_y\{(16\gamma_3 + 9\gamma_2), k_z\} \mp \frac{1}{3}ik_y\{\kappa, k_z\} \mp \frac{12i}{25}k_z(\gamma_2 - \gamma_3)k_z \right] \\ \pm \frac{6i}{25}(\sqrt{3}b - d)(\varepsilon_{xx} - \varepsilon_{zz}) \pm \frac{i}{25}(9\sqrt{3}b + 16d)\varepsilon_{yz},$$

$$C = \frac{\hbar^2}{m_0} k_{-}[\kappa, \hat{k}_z], \quad k_{\pm} = k_x \pm ik_y, \quad \hat{k}_z = -i\frac{\partial}{\partial z}.$$

The built-in strain tensor components for a layer with lattice constant  $a$  in the [013] direction are calculated as follows:

$$\varepsilon_{xx} = \varepsilon_{yy} = \frac{a_0 - a}{a}, \quad \varepsilon_{xz} = 0,$$

$$\varepsilon_{yz} = \frac{12(C_{11} + 2C_{12})(C_{12} - C_{11} + 2C_{44})}{9C_{11}^2 - 9C_{12}^2 + C_{44}(82C_{11} - 18C_{12})} \varepsilon_{xx},$$

$$\varepsilon_{zz} = -\frac{9C_{11}^2 + 18C_{11}(C_{12} - C_{44}) - 27C_{12}^2 + 146C_{44}C_{12}}{9C_{11}^2 - 9C_{12}^2 + C_{44}(82C_{11} - 18C_{12})} \varepsilon_{xx},$$

where  $a_0$  is the lattice constant of a buffer layer, and the  $x$ ,  $y$ , and  $z$  axes are aligned with the (100), (03 -1), and (013) directions, respectively.

TABLE II. Values of the parameters used in calculation (Refs. 10 and 12).

Parameters	CdTe	HgTe	Parameters	CdTe	HgTe
$E_g$ (eV)	1.606	-0.303	$a$ (Å)	6.48	6.46
$E_v$ (eV)	-0.62 <sup>a</sup>	0	$a_c$ (eV)	-2.925	-2.380
$\Delta$ (eV)	0.91	1.08	$a_v$ (eV)	0	1.31
$F$	-0.64 <sup>a</sup>	1.77 <sup>a</sup>	$b$ (eV)	-1.2	-1.5
$E_p$ (eV)	20.8 <sup>a</sup>	20.8 <sup>a</sup>	$D$ (eV)	-5.4	-2.5
$\gamma_1$	1.47	4.1	$C_{11}$ ( $10^{11}$ din/cm <sup>2</sup> )	5.62	5.92
$\gamma_2$	-0.28	0.5	$C_{12}$ ( $10^{11}$ din/cm <sup>2</sup> )	3.94	4.14
$\gamma_3$	0.03	1.3	$C_{44}$ ( $10^{11}$ din/cm <sup>2</sup> )	2.06	2.19
$\kappa$	-1.31	-0.4	-	-	-

<sup>a</sup>Values were adjusted.

The parameters of the materials were taken from Ref. 10 except  $a_c, a_v, b, d$ , and the estimates for the elastic modules  $C_{ij}$ , which were taken from Ref. 12. Table II shows an overview of the different parameters and corresponding values used in the calculations for CdTe and HgTe.

In order to get better agreement of the calculations and experimental data on transition energies we have adjusted some parameters of the model. The first one is the valence band offset (VBO) of CdTe and HgTe. Since there is no way to measure this parameter directly it is usually estimated by matching experimental results and calculations. According to Ref. 13 VBO is  $(570 \pm 60)$  meV. We have used the value 620 meV to fit our results.

The second adjusted parameter is the Kane parameter  $E_p = \frac{2m_0P^2}{\hbar^2}$ . According to the model we use, the wave function of the electron is expanded over the same basis functions in the whole heterostructure.<sup>14</sup> They are Bloch functions of some virtual reference crystal.<sup>15</sup> Hence parameter  $E_p$  depending only on basis functions is also the same for all layers and can be freely adjusted since the reference crystal is chosen arbitrarily.

One should take care to keep other parameters in agreement with  $P$  because bulk conduction band effective mass  $m_c$  must not change. That is why the value of parameter  $F$  was also adjusted for each material according to the following formula:<sup>16</sup>

$$A_C = \frac{\hbar^2}{2m_0}(2F + 1) = \frac{\hbar^2}{2m_c} - \frac{\hbar^2}{3m_0} \frac{E_p}{E_g} - \frac{\hbar^2}{6m_0} \frac{E_p}{(E_g + \Delta)}$$

The  $E_p$  value used was 20.8 eV (instead of 18.8 meV).<sup>13</sup>

#### IV. RESULTS AND DISCUSSION

The first part of this section is devoted to the group of samples with inverted band structures (A and B). For this set of QWs, typical calculated magnetic field dependences of the energies for the lowest LLs in the conduction band and the top LLs in the valence band are plotted in Fig. 3 for sample A. One can see at approximately 6 T the crossing of the lower level of the conduction band ( $n = -2$ ) and the upper level of the valence band ( $n = 0$ ) at the critical field  $B_c$  (indicated by dashed line). Above the crossing field, the topologically insulating phase is transformed into the conventional quantum Hall insulator phase. The magnetic field breaks time-reversal

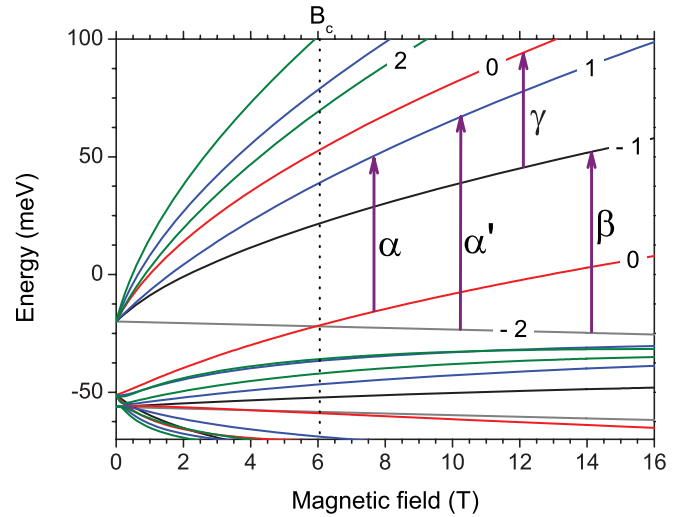


FIG. 3. (Color online) Calculated dispersion of Landau levels for sample A. The expected dominant absorption transitions are denoted by arrows and greek letters. Depending on the LL filling factors, the  $\alpha$ ,  $\alpha'$ ,  $\beta$ , and  $\gamma$  lines should be observable in all samples with band inversion.

symmetry and therefore can open up a gap in the energy spectrum of the edge states. This is a nontrivial consequence of the inverted band structure of the HgTe quantum well.<sup>10</sup>

In Faraday geometry in electro-dipole approximation the transitions are allowed only when the LL number is changed by  $\pm 1$  (for unpolarized radiation). Those transitions are marked with small greek letters.<sup>17</sup> The  $\alpha$  lines in the absorption spectrum relate to the transitions between the LLs  $n = 0$  and  $n = 1$ , the  $\beta$  lines are for the  $n = -2$  to  $n = -1$  level transitions, and the  $\gamma$  lines are for the  $n = -1$  to  $n = 0$  level transitions.

The transition from  $n = -2$  to  $n = 1$  marked as  $\alpha'$  is forbidden by symmetry and cannot be observed in an ideal axially symmetric system. If the symmetry is broken for some reasons the two levels that cross at  $B = B_c$  can interact. Then the level with  $n = -2$  will have an admixture of  $n = 0$  and the  $\alpha'$  transition will be allowed.<sup>7</sup>

The transmission spectra measured in sample A as a function of the magnetic field are plotted in Fig. 4. The spectra show two close peaks indicated by squares and circles, at the calculated positions of the  $\alpha$  transition (for example: 60.4 meV at 6 T, cf. Fig. 5). This double peak behavior can be explained by the avoided crossing of LLs  $n = 0$  and  $n = -2$  due to the nonaxial terms in the Hamiltonian. This can be more clearly seen in Fig. 5. The avoided crossing of these levels was already observed in the same experimental conditions, in 8-nm-wide [001] oriented HgTe quantum wells and was attributed to the bulk inversion asymmetry of zinc blende compounds.<sup>7</sup> However, in our sample the observed splitting is larger (approximately 5.5 meV versus 4 meV in Ref. 7). That can be attributed to the lower symmetry of the [013] growth direction.

The peak positions of the observed transitions in sample A ( $d = 8$  nm), are plotted in Fig. 5 as a function of the applied magnetic field. Samples are completely opaque in the range of the reststrahlen bands (indicated by shaded areas between

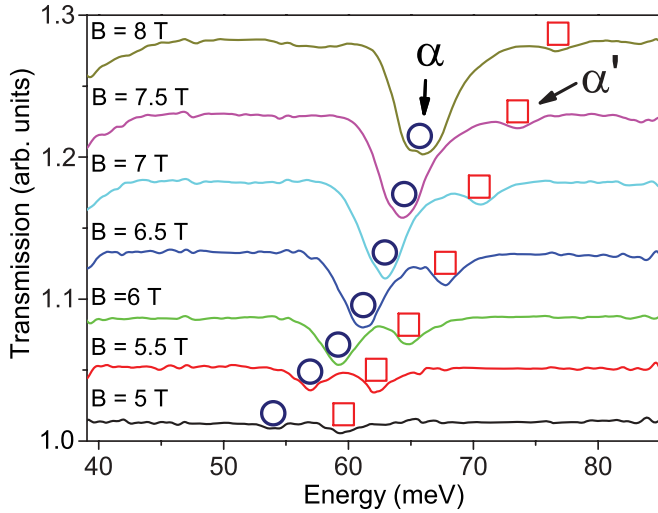


FIG. 4. (Color online) Measured transmission spectra of sample A in a relevant range of magnetic fields. The  $\alpha$  transition shows a double peak behavior close to a critical magnetic field  $B_c = 6$  T. The spectra are vertically shifted for the sake of clarity.

16 and 21 meV for HgTe/Cd<sub>x</sub>Hg<sub>1-x</sub>Te and between 30 and 37 meV for GaAs substrate). Solid lines show the expected excitation energies following the calculation presented above. Dashed lines show the same energies for parameters from Ref. 10. One can see at low magnetic fields (up to 3 T) an absorption line indicated by full squares, having a linear behavior with  $B$ . This line is attributed to the cyclotron

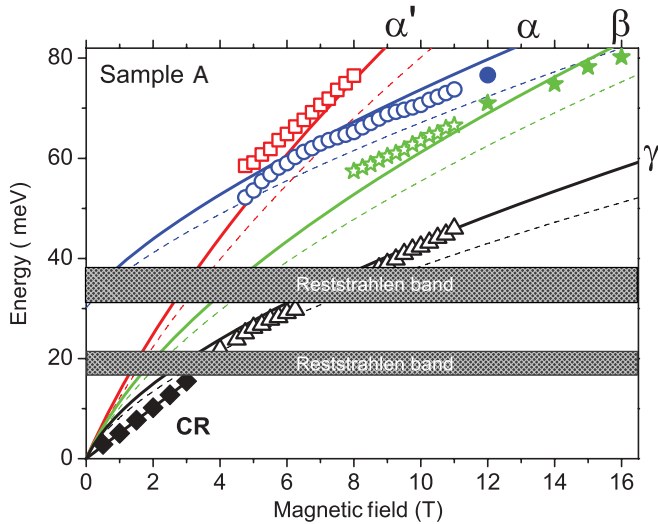


FIG. 5. (Color online) Peak positions of the observed transitions in sample A, plotted as a function of the applied magnetic field. The shaded areas are the reststrahlen bands. Solid lines show the expected excitation energies following the calculation presented above with adjusted parameters. Dashed lines show the same energies for parameters from Ref. 10. The  $\alpha$  transition (squares and circles) shows a double component character in the vicinity of the crossing fields  $B_c$ . The intraband  $\beta$  transition (stars) is also seen above 8 T. The cyclotron resonance (CR) absorption is linear with  $B$ . The last transition visible from 4 up to 11 T is usually denoted as  $\gamma$  transition (triangles). The full symbols correspond to experimental points obtained at higher magnetic fields in Montpellier Teralab.

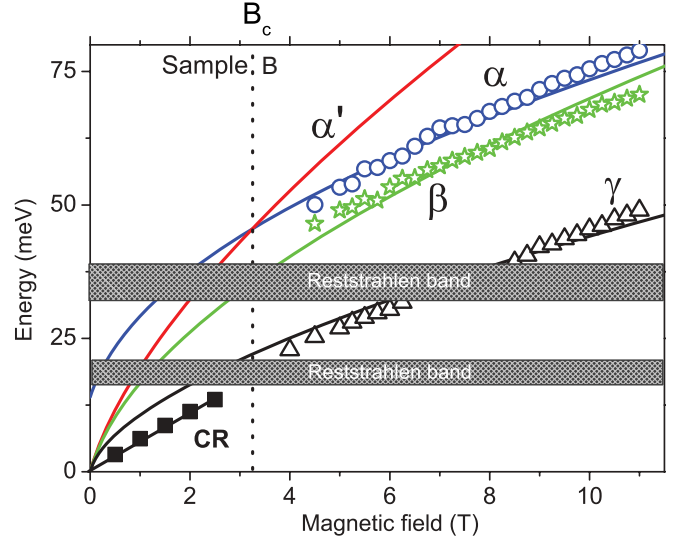


FIG. 6. (Color online) Peak positions of the observed transitions in sample B, as a function of the applied magnetic field. The double component of the  $\alpha$  transition is not seen close to the expected crossing field  $B_c$ . The intraband  $\beta$  transition is seen above 4.5 T and the cyclotron resonance (CR) absorption is linear with  $B$ . The  $\gamma$  transition is also visible from 4.5 to 11 T.

resonance (CR) absorption in the 2D electron gas at LL filling factor  $\nu \gg 1$ . From the linear fitting of this line, the effective mass of carriers is found to be  $m^* = eB/\omega_C = 0.022m_0$ . The line starting from 4 T indicated by empty triangles, corresponds to the transition from LLs  $n = -1$  to  $n = 0$  in the conduction band, which is usually denoted as the  $\gamma$  transition.<sup>7,9</sup> In high magnetic fields this transition should vanish when the Fermi level crosses LL  $n = -1$ . For a dark concentration of  $2.5 \times 10^{11}$ , the LL filling factor equals 1 at 10 T. In the conditions of our magnetospectroscopy measurements without controllable lighting, the carrier concentration in these samples could have changed as compared to the initially measured dark concentrations. We assume that the lighting increases the concentration (cf. Ref. 6), and the value of the magnetic field where the transition vanishes is not reached in magnetic fields up to the 11 T available in Grenoble. Therefore we consider that these two lines separated by the reststrahlen band of the GaAs substrate correspond to the same  $\gamma$  transition. The intraband  $\beta$  line, indicated by stars, corresponding to the transition from LLs  $n = -2$  to  $n = -1$ , is also seen above 8 T, up to 16 T. The full stars and circles correspond to experimental points obtained at higher magnetic fields in the Montpellier Teralab. The  $\alpha$  and  $\alpha'$  lines, showing an anticrossing behavior around the critical field  $B_c = 6$  T and the energy of 60 meV are indicated by empty circles and empty squares, respectively, from 4.5 up to 12 T. All these experimental results are in good agreement with our calculations. The  $\alpha$  line becomes visible in magnetic field over 5 T when the LL filling factor is well below 3 and the  $\beta$  line becomes visible over 8 T where the LL filling factor is well below 2, when the corresponding final LLs for the transitions under consideration are partially unoccupied.

In Fig. 6, the peak positions of the observed transitions are plotted for sample B ( $d = 7$  nm). The  $\alpha$ ,  $\beta$ , and  $\gamma$  transition lines are visible. The shaded areas are again the

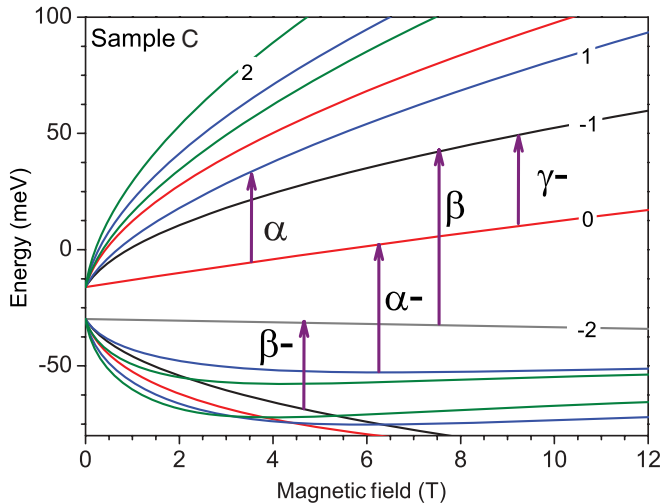


FIG. 7. (Color online) Calculated dispersion of Landau levels for sample C. The expected dominant absorption transitions are denoted by arrows and greek letters. The  $\alpha$ ,  $\alpha-$ ,  $\beta$ ,  $\beta-$ , and  $\gamma-$  lines have energies that are in the spectral range of our measurements.

reststrahlen bands. The cyclotron resonance line (full squares) and  $\gamma$  transition (empty triangles) are visible at approximately the same magnetic field values as in sample A. The  $\beta$  transition (empty stars) can be followed from 4.5 up to 11 T showing like the  $\gamma$  line, a very good agreement with theory. Because of the lower electron concentration, this transition appears at smaller magnetic field if compared with the sample A (see Fig. 4). Therefore the final state for  $\beta$  transition, LL  $n = -1$ , starts to depopulate in lower magnetic fields. The circles also visible from 4.5 up to 11 T are attributed to the  $\alpha$  transition. For this thickness, the calculated crossing field  $B_c$  is about 3.25 T. At this field the ending level of the  $\alpha$  transition is filled with electrons and the transition is forbidden by the Pauli principle, so the expected double peak character of the  $\alpha$  transition close to this critical field cannot be seen in this sample.

Even if these two samples have inverted band structures, only one of them (A) shows an anticrossing behavior around the calculated critical field. However, for both of them the experimental results are in very good agreement with theory for all visible transitions. Therefore, we assume that with well adapted electron concentration, sample B should exhibit an anticrossing of the zero-mode LLs at the critical field  $B_c = 3.25$  T, above which the topologically insulating phase is transformed into the conventional quantum Hall insulator phase.<sup>4</sup>

The two samples (C and D) of the second group studied in the rest of the paper have noninverted band structure and consequently, have no topological insulator behavior. However, the quantum well width of both samples is close to the critical thickness and massless Dirac fermions should be observable with a square root behavior of the transition energy as a function of the magnetic field.

Calculated magnetic field dependences of the energies for the lowest LL in the conduction band and top LL in the valence band, that are expected to be observed in noninverted structures, are plotted in Fig. 7 (calculated for parameters of sample C). The  $\alpha$  and  $\alpha-$  lines in the absorption spectrum

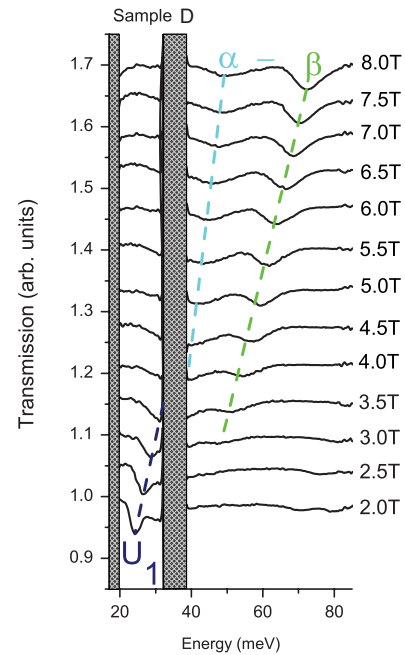


FIG. 8. (Color online) Measured transmission spectra of sample D. The notation of the observed lines is in agreement with the transitions assignment used in Fig. 7.  $U_1$  corresponds to an unknown transition line. The shaded areas are the reststrahlen bands. The spectra are vertically shifted for the sake of clarity.

relate to the transitions for the LLs  $n = 1$  to  $n = 0$  and for  $n = 0$  to  $n = 1$ , respectively. The  $\beta$  lines are for the  $n = -2$  to  $n = -1$  level transitions, the  $\beta-$  lines are for the  $n = -1$  in the valence band to  $n = -2$  level transitions, and the  $\gamma-$  lines are for the  $n = 0$  to  $n = -1$  level transitions. We want to point out that the  $\beta-$  transition is observable only in  $p$ -type samples and cannot take place simultaneously with  $\gamma-$ .

The transmission spectra measured in sample D ( $d = 5.9$  nm) as a function of the magnetic field from 2 up to 8 T are plotted in Fig. 8. The  $\alpha-$ , (from 40 to 50 meV) and  $\beta$  (from 50 to 70 meV) transition lines are visible. An unknown line at low magnetic fields, between 25 and 32 meV, is also visible and is called  $U_1$ . The dashed lines are guides for the eye and the shaded areas are the reststrahlen bands.

Figure 9(a) shows the positions of observed transitions in sample D versus the magnetic field. On the contrary of the LL filling factor, the  $\alpha$  transition is not observed in these spectra and the  $\alpha-$  line (empty pentagons) can be seen below and above the reststrahlen bands, from 0.5 up to 11 T. Both samples from the second group proved to exhibit negative photoconductivity under lightning in contrast to the samples from the first group. The dark concentration in this sample is about  $2.8 \times 10^{10} \text{ cm}^{-2}$  and under uncontrollable lightning the Fermi level can go to the forbidden gap, so only interband ( $\alpha-$  and  $\beta$ ) transitions could be observed. As seen in Fig. 9(a) the calculated  $\alpha-$  and  $\beta$  transitions are the best to fit our experimental results. Unknown line  $U_1$  (the strongest line of the spectra, represented by empty triangles) can also be seen from very low magnetic fields (0.3 T) up to 3.5 T below the second reststrahlen band; its possible origin will be discussed later. Another unknown line called  $U_2$ , is visible from 3 to 11 T and one can also see it in Fig. 9(b) represented by

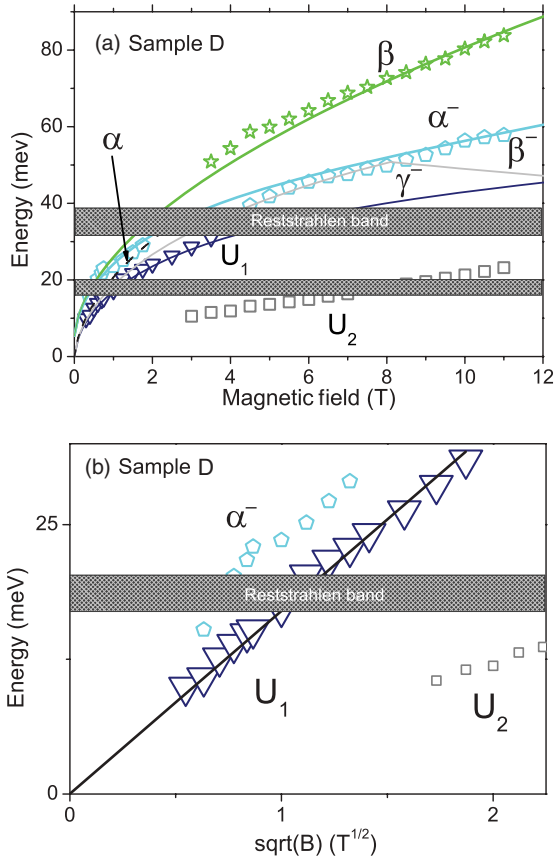


FIG. 9. (Color online) (a) Peak positions of the observed transitions in sample D. The  $\beta$  (empty stars), and  $\alpha^-$  (empty pentagons) transitions are observed in good agreement with theory represented by the solid lines. Two other transitions called  $U_1$  and  $U_2$  are observed (represented, respectively, by empty triangles and squares). (b) Peak positions of the transitions as a function of the square root of the magnetic field. The  $U_1$  transition exhibits a square root dependence on B up to 4 T.

empty squares. In the authors' opinion, this low-frequency line could be related to  $1s \rightarrow 2p$  transitions of shallow donor impurities.

By plotting the positions of the transitions as a function of the square root of the magnetic field, one can clearly see in Fig. 9(b) a square root dependence of the  $U_1$  transition on the magnetic field, as expected in the single-particle model of massless Dirac fermions. Unlike in our experiments, Dirac fermions in HgTe QW structures have been observed recently by magnetotransport measurements. These results are reported in Ref. 18, where quantum Hall plateaus exhibit the anomalous sequence characteristic of Dirac systems.

Figure 10(a) shows the positions of observed transitions versus the magnetic field in sample C ( $d = 5.6$  nm). As in Fig. 9 for sample D, the  $\alpha^-$  (empty pentagons) and  $\beta$  (empty stars) transition lines are also visible in the second sample of the noninverted group (C). The unknown line  $U_1$  (empty triangles) is also visible in this sample from 2 to 4.5 T. The  $\alpha^-$  transition is visible above the reststrahlen band up to 11 T. The  $\beta$  transition can be followed from 4 up to 9 T with good agreement with our calculations. The  $U_1$  transition is also visible below the reststrahlen band, down to low fields (0.6 T).

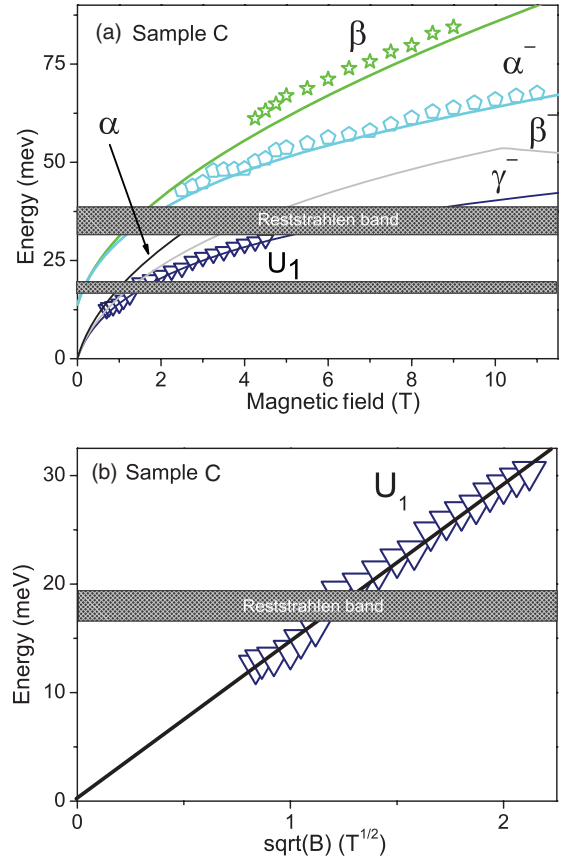


FIG. 10. (Color online) (a) Peak positions of the observed transitions in the noninverted sample C. The  $\alpha^-$  (pentagons) and  $\beta$  (stars) transitions are observed in good agreement with theory represented by the straight lines. Another transition called  $U_1$  represented with triangles is observed at low energies. (b) Peak positions of the transitions as a function of the square root of the magnetic field. The  $U_1$  transition exhibits a square root dependence on B up to 5 T.

The positions of the transitions as a function of the square root of the magnetic field are plotted in Fig. 10(b). One can clearly see the same square root dependence of the  $U_1$  transition on the magnetic field, as in sample C [see Fig. 9(b)], as expected for the linear dispersion of the massless Dirac fermions.

The measurements performed in the four samples with QW thickness around the critical value allowed us to track the evolution of the magneto-optical response from a narrow-gap semiconductor with very light but still massive carriers to a Dirac-type system with massless fermions. In both samples with noninverted structures, C and D, one can see a good agreement between the experimental positions of the  $U_1$  line and the theoretical calculations of the  $\gamma^-$  line. However, even without considering that  $\alpha$  transition is not observed either, the oscillator strength of the  $\gamma^-$  transition line is five orders of magnitude lower than those for  $\alpha^-$  and  $\beta$  transitions, and as a consequence, this transition should not be observed in our experimental configuration. On the other hand, the theoretical transition line  $\beta^-$  could also fit the experimental data of the  $U_1$  line. The oscillator strength of  $\beta^-$  is comparable with the other visible lines as  $\alpha^-$  and  $\beta$ . Moreover, in both samples the  $\beta^-$  transition is vanishing when the  $\beta$  transition is appearing, as

expected if the Fermi level crosses the LL  $n = -2$ . However, the agreement between theory and experiment is not very good in both samples and this is the reason why we cannot confirm that  $U_1$  corresponds to  $\beta-$ . Another possibility is that instead of  $\gamma-$  or  $\beta-$  transitions, the observed  $U_1$  line corresponds to a transition between impurity/defect states bound to the related Landau levels. The fluctuations of the QW width (about one monolayer) could also result in violation of cyclotron resonance selection rules in the second group of samples with the most narrow QWs, thus making possible the observation of the forbidden inter-LL transitions. Obviously, the above approach to interpret the data does not take into account all possible effects that may influence the measured spectra. A full quantitative interpretation of our results requires more complete theoretical and experimental developments. Nevertheless, the  $U_1$  transition line shows unambiguously in both noninverted structures a square root behavior on magnetic field (cf. Figs. 9 and 10), corresponding to the linear dispersion of the massless Dirac fermions in HgTe QWs.

## V. CONCLUSIONS

We have experimentally studied far-infrared Landau level transitions spectra under magnetic field in a series of HgTe/Cd<sub>x</sub>Hg<sub>1-x</sub>Te [0 1 3] QW heterostructures around the

critical thickness. Both intraband and interband magnetoabsorption have been investigated in quantizing magnetic fields up to 16 T. We have confirmed the observation of the crossing of the zero-mode Landau levels caused by the breaking of time-reversal symmetry, expected in two-dimensional topological insulators. We have shown very good agreement between the experimental data and the Landau levels transition energies calculated using the  $8 \times 8$  Kane model. We have also shown the linear dispersion of the massless Dirac fermions in HgTe QW structures, by the square root behavior of LLs on magnetic field.

## ACKNOWLEDGMENTS

This work was supported by CNRS and GDR-I project “Semiconductor sources and detectors of THz frequencies,” and by the Scientific Council of Montpellier II University via the “Nanosciences” grant. We acknowledge the Region of Languedoc–Roussillon through the “Terahertz Platform” project. The work was also supported by the Polish Ministry of Science and Higher Education, via Project No. N202/103936, by the Russian Foundation for Basic Research (Grants No. 11-02-00958, No. 11-02-97061, and No. 11-02-93111), and by the Russian Academy of Sciences. We finally thank Petre Buzatu and Christian L’henoret for technical support.

\*Corresponding author: frederic.teppe@univ-montp2.fr

<sup>1</sup>C. L. Kane and E. J. Mele, *Phys. Rev. Lett.* **95**, 146802 (2005).

<sup>2</sup>M. Z. Hasan and C. L. Kane, *Rev. Mod. Phys.* **82**, 3045 (2010).

<sup>3</sup>B. Andrei Bernevig, T. L. Hughes, and S.-C. Zhang, *Science* **314**, 1757 (2006).

<sup>4</sup>M. König, S. Wiedmann, C. Brüne, A. Roth, H. Buhmann, L. W. Molenkamp, X.-L. Qi, and S.-C. Zhang, *Science* **318**, 766 (2007).

<sup>5</sup>A. H. Castro Neto, F. Guinea, N. M. R. Peres, K. S. Novoselov, and A. K. Geim, *Rev. Mod. Phys.* **81**, 109 (2009).

<sup>6</sup>A. V. Ikonnikov, M. S. Zholudev, K. E. Spirin, A. A. Lastovkin, K. V. Maremyanin, V. Ya. Aleshkin, V. I. Gavrilenko, O. Drachenko, M. Helm, J. Wosnitza, M. Goiran, N. N. Mikhailov, S. A. Dvoretiskii, F. Tepe, N. Diakonova, C. Consejo, B. Chenaud, and W. Knap, *Semicond. Sci. Technol.* **26**, 125011 (2011).

<sup>7</sup>M. Orlita, K. Masztalerz, C. Faugeras, M. Potemski, E. G. Novik, C. Brune, H. Buhmann, and L. W. Molenkamp, *Phys. Rev. B* **83**, 115307 (2011).

<sup>8</sup>S. Dvoretzky, N. Mikhailov, Y. U. Sidorov, V. Shvets, S. Danilov, B. Wittman, and S. Ganichev, *J. Electron. Mater.* **39**, 918 (2010).

<sup>9</sup>K. von Klitzing and G. Ebert, in *Two-Dimensional Systems, Heterostructures, and Superlattices*, edited by G. Bauer, F. Kuchar, and H. Heinrich (Springer-Verlag, Berlin, Heidelberg, New York, Tokyo, 1984), p. 242.

<sup>10</sup>E. G. Novik, A. Pfeuffer-Jeschke, T. Jungwirth, V. Latussek, C. R. Becker, G. Landwehr, H. Buhmann, and L. W. Molenkamp, *Phys. Rev. B* **72**, 035321 (2005).

<sup>11</sup>J. Los, A. Fasolino, and A. Catellani, *Phys. Rev. B* **53**, 4630 (1996).

<sup>12</sup>K. Takita, K. Onabe, and S. Tanaka, *Phys. Status Solidi B* **92**, 297 (1979).

<sup>13</sup>C. R. Becker, V. Latussek, A. Pfeuffer-Jeschke, G. Landwehr, and L. W. Molenkamp, *Phys. Rev. B* **62**, 10353 (2000).

<sup>14</sup>M. G. Burt, *J. Phys.: Condens. Matter* **4**, 6651 (1992).

<sup>15</sup>B. A. Foreman, *Phys. Rev. B* **72**, 165345 (2005).

<sup>16</sup>B. A. Foreman, *Phys. Rev. B* **56**, R12748 (1997).

<sup>17</sup>M. Schultz, U. Merkt, A. Sonntag, U. Rossler, R. Winkler, T. Colin, P. Helgesen, T. Skauli, and S. Løvold, *Phys. Rev. B* **57**, 14772 (1998).

<sup>18</sup>B. Büttner, C. X. Liu, G. Tkachov, E. G. Novik, C. Brüne, H. Buhmann, E. M. Hankiewicz, P. Recher, B. Trauzettel, S. C. Zhang, and L. W. Molenkamp, *Nat. Phys.* **7**, 418 (2011).